

# Mid-infrared plasmons in scaled graphene nanostructures

Hugen Yan<sup>1\*†</sup>, Tony Low<sup>1†</sup>, Wenjuan Zhu<sup>1</sup>, Yanqing Wu<sup>1</sup>, Marcus Freitag<sup>1</sup>, Xuesong Li<sup>1</sup>,

Francisco Guinea<sup>2</sup>, Phaedon Avouris<sup>1\*</sup> and Fengnian Xia<sup>1\*</sup>

<sup>1</sup>*IBM Thomas J. Watson Research Center, Yorktown Heights, NY 10598*

<sup>2</sup>*Instituto de Ciencia de Materiales de Madrid. CSIC. Sor Juana Inés de la Cruz 3. 28049 Madrid, Spain*

**Plasmonics takes advantage of the collective response of electrons to electromagnetic waves, enabling dramatic scaling of optical devices beyond the diffraction limit. Here, we demonstrate the mid-infrared (4 to 15  $\mu\text{m}$ ) plasmons in deeply scaled graphene nanostructures down to 50 nm, more than 100 times smaller than the on-resonance light wavelength in free space. We reveal, for the first time, the crucial damping channels of graphene plasmons via its intrinsic optical phonons and scattering from the edges. A plasmon lifetime of 20 femto-seconds and smaller is observed, when damping through the emission of an optical phonon is allowed. Furthermore, the surface polar phonons in  $\text{SiO}_2$  substrate underneath the graphene nanostructures lead to a significantly modified plasmon dispersion and damping, in contrast to a non-polar diamond-like-carbon (DLC) substrate. Much reduced damping is realized when the plasmon resonance frequencies are close to the polar phonon frequencies. Our study paves the way for applications of graphene in plasmonic waveguides, modulators and detectors in an unprecedentedly broad wavelength range from sub-terahertz to mid-infrared.**

<sup>†</sup>These authors contributed equally to the work.

\*Email: [hyan@us.ibm.com](mailto:hyan@us.ibm.com) (H.Y.), [avouris@us.ibm.com](mailto:avouris@us.ibm.com) (P.A.) and [fxia@us.ibm.com](mailto:fxia@us.ibm.com) (F.X.)

## **Introduction**

Plasmonic nanostructures allow the confinement of electromagnetic energy beyond the diffraction limit, enabling applications ranging from metamaterials, quantum optics, and photovoltaics to photodetectors and biological sensing<sup>1</sup>. In particular, graphene based plasmonics has garnered intense interests due to its unique tunability<sup>2-8</sup> and presumably long plasmon lifetime<sup>2,9</sup> and high degree of electromagnetic confinement<sup>6,7</sup>. The electromagnetic response of patterned graphene micro-structures in the terahertz frequency regime was studied recently<sup>4,8,9</sup>, and was found to be dominated by the plasmon excitations of Dirac fermions<sup>4,8</sup>. Here we demonstrate that the dispersive nature of the 2-dimensional plasmon enables engineering of graphene plasmon resonances into the mid-IR regime by patterning graphene into nanostructures down to 50 nanometers. In contrast to their microstructure counterparts, whose plasmon resonances are in the terahertz frequency range, the mid-IR plasmonic response has been found to be affected strongly by interactions with substrate phonons and the graphene intrinsic optical phonons. These interactions lead to the renormalization of the plasmon dispersion and govern the lifetimes of plasmons. Moreover, an edge related effect on the mid-IR plasmonic responses is explicitly identified, which complements not only the extensive electronic transport studies performed previously on similar graphene nanostructures<sup>10-12</sup>, but also the research field concerning plasmons in metal cluster<sup>13,14</sup>.

## **Experiments and methodology**

Graphene nanostructures such as nanoribbon, antidot and nanodisk arrays are defined using electron-beam lithography on chemical-vapor-deposition (CVD) grown graphene<sup>15</sup>.

Different supporting substrates such as  $\text{SiO}_2$  and DLC<sup>16</sup> are used on top of highly resistive silicon wafers. The mid-IR transmission measurement scheme is shown in Fig. 1a. The setup consists of an IR microscope coupled to a Fourier transform infrared spectrometer (FTIR), used in conjunction with a broadband polarizer. Details of the nanofabrication and infrared measurement are outlined in the Methods section.

The qualitative behaviour of plasmonic response in graphene nanoribbons and nanodisks are similar, except for a distinct polarization dependence in the former<sup>4,8</sup>. In this paper, we focus on graphene nanoribbons, where a typical scanning electron micrograph is displayed in Fig. 1b. The electromagnetic responses of these graphene nanoribbon arrays are characterized by their extinction spectra  $1-T_{\text{per}}/T_0$  or  $1-T_{\text{||}}/T_0$ , where  $T_{\text{per}}$  ( $T_{\text{||}}$ ) is the transmission through the ribbon array of the light with electric field perpendicular (parallel) to the ribbon, and  $T_0$  is the transmission through the substrate without graphene (but with  $\text{SiO}_2$  or DLC). Fig. 1c shows the extinction spectra of a ribbon array on  $\text{SiO}_2$  substrate, with widths of around 240 nanometers. The two curves correspond to incident light with polarization perpendicular (red) and parallel (grey) to the ribbons, respectively.

Due to the excitation of localized plasmons, the extinction spectrum with perpendicular polarization has prominent resonance peaks<sup>4,8</sup>. The multiple resonance peaks observed here are in sharp contrast to the far-IR spectra of graphene microstructures, which usually display a single strong resonance<sup>4,8</sup>. Without plasmon excitations, the spectrum with parallel polarization lacks resonance peaks except for small features from  $1000\text{ cm}^{-1}$  to  $1200\text{ cm}^{-1}$ . These features are related to the fast-varying dynamic dielectric function of

the SiO<sub>2</sub> substrate<sup>17</sup>, and weak (< 1% in extinction) compared to the prominent plasmon peaks. In this mid-IR wavelength range, if the light polarization is parallel to the highly doped graphene ribbons (as reported in this work), their interaction is insignificant due to the Pauli blocking of interband transitions and the weakness of the free-carrier intraband transitions in such high frequencies<sup>18</sup>. As a result, the transmission spectra of the ribbons for the parallel polarized light ( $T_{//}$ ) are very close to the reference ( $T_0$ ) and in subsequent presentations will serve as reference for the extinction spectra in the case of perpendicularly polarized light. In other words, the extinction spectrum is defined as  $1 - T_{per}/T_{//}$  subsequently (See Methods).

The multiple resonance structures observed in the spectra of Fig. 1c are due to the interactions of graphene plasmons with the substrate phonons, as we will show in subsequent discussions. In fact, the Fuchs-Kliwer<sup>19</sup> surface-optical (SO) phonons are well-known in polar semiconductor surfaces and have been extensively studied in conventional 2-dimensional electron systems<sup>20,21</sup>. When graphene is placed on a polar substrate (e.g. SiO<sub>2</sub>) accommodating these SO phonons, the long-range Fröhlich coupling can mediate interactions with the electronic degrees of freedom in graphene<sup>22,23</sup>, including the collective plasmon modes<sup>24</sup>. These interactions produce hybridized plasmon-phonon modes in the vicinity of their crossing energies and were recently observed by different techniques such as electron-energy loss spectroscopy in epitaxial graphene on SiC substrate<sup>25</sup> and near-field optical nanoscopy of graphene on SiO<sub>2</sub> substrate<sup>5</sup>. Before we present extended studies of these hybridized plasmon-phonon

modes, it is instructive to first consider a simpler system, i.e., graphene on a non-polar substrate DLC.

### **Plasmons of graphene nanoribbons on DLC substrate**

Fig. 2a shows the extinction spectra of graphene ribbons with various widths  $W$  on a DLC substrate. Indeed, there is only one prominent plasmon resonance peak for each spectrum, unlike the spectra on  $\text{SiO}_2$  substrate. Here, we would expect that the plasmon resonance frequency follows a simple  $\sqrt{q}$  dispersion in the long wavelength limit, with  $q$  being the plasmon wave-vector, as predicted by the Random Phase Approximation (RPA) theory for the linear response of a 2-dimensional electronic systems<sup>26</sup> and graphene<sup>27,28</sup>. For localized plasmons in graphene ribbons,  $q$  is simply given by  $\pi/W$ <sup>29</sup>. The inset of Fig. 2a shows the extracted plasmon frequencies from Fig. 2a as a function of  $\pi/W$ , where salient disagreement exists when compared to the simple scaling  $\omega_{pl} \propto \sqrt{\pi/W}$  predicted by theory. This discrepancy cannot be due to the breakdown of the long wavelength approximation, because the wave-vector here is two orders of magnitude smaller than the Fermi wave-vector  $k_f$ . Correction due to quantum confinement effect is also negligible for dimensions larger than 10 nm<sup>30</sup>.

Prior experiments with graphene nanoribbons have shown that it is often necessary to postulate an electrical width smaller than its physical width in order to explain their electrical transport behavior<sup>10-12</sup>. Indeed, fabrication of graphene ribbons by e-beam lithography and oxygen plasmon etching can impart atomic scale defects and complicated edge chemistry<sup>31</sup> that renders the edges electrically “inactive”<sup>32</sup>. In a similar fashion, we

introduce an effective ribbon width defined as  $W_e = W - W_0$ . Fig. 2b displays the plasmon frequency as a function of  $q = \pi/W_e$ . The dashed lines are  $\sqrt{q}$  fittings, which now agree very well with the experiments for two different doping levels, if  $W_0 = 28$  nm is chosen. Using this methodology with the same  $W_0$ , we can also consistently explain the more complicated hybrid plasmon-phonon dispersions in graphene on SiO<sub>2</sub>, to be discussed in the next section.

### Plasmons of graphene nanoribbons on SiO<sub>2</sub> substrate

Fig. 3a shows the extinction spectra for graphene ribbons on SiO<sub>2</sub> substrate with  $W$  ranging from 60 to 240 nm, where we have labeled the three major resonance peaks and a weak higher order resonance<sup>9</sup> within our measured frequency range of 650 to 6000 cm<sup>-1</sup>. We identify four key features in the observed spectra: (1) **Dispersion**: all resonance peaks blue-shift as  $W$  decreases but at very different rates. In particular, peak 3 disperses up in frequency at a much faster rate. (2) **Spectral weights**: The spectral weight transfers from peak 1 to peak 2 and 3 with decreasing  $W$ , and eventually peak 3 retains all of the spectral weight for  $W < 90$  nm. (3) **Linewidths**: the resonance linewidth for peak 3 increases with decreasing  $W$ , while those of peaks 1 and 2 remain almost constant. In fact, the resonance linewidth for ribbons on DLC discussed in previous section also exhibits the same trend as that of peak 3 in Fig. 3a. The linewidth is directly related to the plasmon damping and will be covered in detail in the following section. (4) **Line shape**: peak 3 is very asymmetric, especially for relatively narrow ribbons. As detailed in the Supplementary Information, the line shape can be well described by the Fano resonance model<sup>33</sup>.

The multiple resonances observed in the spectra are due to the plasmon-phonon coupled modes and can be described within a generalized RPA theory<sup>24,34,35</sup>. Directly relevant to our experiments is the loss function  $\Im[1/\epsilon_r^{rpa}]$ , defined as the imaginary part of the inverse dielectric function, which describes the ability of the system to dissipate energy via plasmon excitations. Our calculations include both interactions with the relevant substrate SO phonons<sup>17</sup> at  $\omega_{sp1} = 806\text{cm}^{-1}$  and  $\omega_{sp2} = 1168\text{cm}^{-1}$  and the graphene intrinsic optical phonon modes<sup>36</sup> at  $\omega_{op} = 1580\text{cm}^{-1}$ . Detailed description of the theory is provided in Supplementary Information.

Fig. 3b shows an intensity plot of the loss function overlaid on the extracted resonance peak frequencies obtained from the spectra in Fig. 3a. We applied the same methodology used in previous section, i.e., defining the wave-vector of the localized plasmon to be  $q = \pi/(W-W_0)$ , with the same  $W_0 = 28$  nm. Excellent agreement with the experimentally observed plasmon-phonon dispersions can be obtained using Fröhlich coupling strength of  $F_{sp1}^2 \sim 0.2\text{meV}$  and  $F_{sp2}^2 \sim 2\text{meV}$ , where the latter includes the mode's double degeneracy. The Fröhlich coupling quantifies the hybridization of the plasmon-phonon mode and their anti-crossing energy splitting and is defined as  $F_{sp}^2 = \frac{\hbar\omega_{sp}}{2\pi} (\frac{1}{\epsilon_{high} + \epsilon_0} - \frac{1}{\epsilon_{low} + \epsilon_0})$  in the model (see Supplementary Information), where  $\epsilon_{high}$  ( $\epsilon_{low}$ ) is the high (low) frequency dielectric constant of SiO<sub>2</sub>. The values extracted from fitting of the hybrid plasmon-phonon dispersions, although of the same order as quoted values used in the literatures<sup>37,38</sup>, can serve as a better estimate. In addition, the second order dipolar

mode<sup>9,29</sup> with wave-vector given by  $q = 3\pi/(W-W_0)$  also coincides with the dispersion of its fundamental mode. The above agreement further validates the premise that the effective width  $W - W_0$  defines the plasmon momentum, with a  $W_0 = 28$  nm consistently explains both plasmon and hybrid plasmon-phonon dispersions on both DLC and SiO<sub>2</sub> substrates, respectively.

Furthermore, we note that the loss function can also capture the plasmon peak intensity evolution for the three hybrid plasmon-phonon branches, featuring two anti-crossings and spectral weight transfer from the low frequency to high frequency plasmon branch (peak 3) with increasing  $q$ . See also Supplementary Information.

### **Origins of the Plasmon Damping**

Many plasmonic applications can benefit from a long plasmon lifetime<sup>1</sup>. However, depending on the system of interest, plasmon can decay into photons via radiative processes<sup>39</sup>, into electron-hole pairs via inter- or intra-band Landau damping<sup>35</sup>. In addition, inelastic scattering with phonons<sup>14,40</sup> and elastic carrier scattering processes<sup>9,14</sup> can also contribute to the plasmon damping. The former two processes can be ruled out since contribution from radiative damping in graphene nanostructures is expected to be negligible<sup>8,9</sup> and that plasmon excitations in our devices lie outside of the Landau damping regime, as indicated in the Fig. 2b and Fig. 3b. However, the latter two processes can be important with large plasmon energies (i.e.  $\hbar\omega_{pl} > 0.2eV$ ) and small dimensions respectively. Lastly, interactions with the SO phonons can also influence the lifetimes of the hybrid plasmon-phonon modes, especially when the energy of the hybrid



mode is close to that of the SO phonons<sup>41</sup>. Our scaled graphene nanoribbons with different widths enable us to identify the damping mechanisms of graphene plasmons for the first time in a comprehensive manner.

From the extinction spectra in Fig. 2a and 3a, the plasmon damping rate  $\Gamma_p$  can be extracted from the resonance linewidth using a simple procedure as described in the Supplementary Information. Figure 4a plots the extracted  $\Gamma_p$  as a function of the effective ribbon width  $W_e$ . For the hybrid plasmon-phonon modes on SiO<sub>2</sub>, only peak 3 is plotted since it exists for all of the different size ribbons and its damping rate evolves dramatically. We analyze first the extracted  $\Gamma_p$  for DLC case. Since its plasmon resonance energy is below the optical phonon energy, the dominant broadening mechanism involves the elastic carrier scattering processes. Indeed, its damping rate increases as  $W_e$  decreases, indicative of scattering at the edges of the ribbon. Similar damping effect for plasmons in metallic nanoparticles has been extensively studied<sup>13,14</sup>. This effect can be modeled using<sup>13,14</sup>  $\Gamma_p = \Gamma_0 + a / W_e$ , where  $\Gamma_0$  is the damping rate due to the carrier scattering in bulk graphene which was measured to be about 69 cm<sup>-1</sup> from the Drude response<sup>18</sup> of large area, unpatterned graphene nearby on the same DLC substrate and  $a$  is a fitting parameter. The same formalism was used to describe the damping in metal nanoparticles. Here we also want to emphasize that in micro-scale plasmonics structures, the damping rate  $\Gamma_0$  is almost identical to that extracted from Drude response, indicating the negligible impact of the edges in micro-scale structures. In the fit,  $a \approx 2 \times 10^6 \text{ m/s}$ , of the order of Fermi velocity, as expected from the edge scattering point of view. Lastly, we note that, in principle, the inhomogeneity of the

ribbon width may also lead to an apparent resonance broadening effect; however, estimates based on the SEM characterization, the doping dependence and ribbon width dependence of the plasmon peak broadening for the ribbons on DLC substrate, all suggest the negligible contribution of the inhomogeneity, see Supplementary Information.

Despite similar characteristics of nanoribbons fabricated using CVD graphene (i.e. similar  $\Gamma_0$  and doping), the plasmon damping of ribbons on  $\text{SiO}_2$  are different from its DLC counterpart as shown in Fig. 4a. First, we emphasize that the damping of hybrid plasmon-phonon modes also depends on its relative plasmon versus phonon character. For example, the mode described by peak 3 in Fig. 3a is predominantly phonon-like for large  $W_e$  since it resonates near the SO phonon frequency  $\omega_{sp2}$ . As a result, its damping is determined by the SO phonon lifetime instead (see Supplementary Information), which typically is in the picosecond regime. This explains the lower damping rate of this mode compared to the DLC case in the large  $W_e$  limit, as shown in Fig. 4a for  $W_e > 120$  nm. Similarly, the small linewidths for peaks 1 and 2 in Fig. 3a can also be accounted for by the same reasoning. On the other hand, for narrower ribbons (i.e.  $W_e < 90$  nm), the mode described by peak 3 disperses rapidly in frequency and becomes predominantly plasmon-like. However, in contrast to the DLC counterpart, it has a plasmon frequency larger than the graphene optical phonon frequency of  $1580 \text{ cm}^{-1}$ . Therefore, the plasmon can decay into electron-hole pair via the emission of a graphene optical phonon, which might explain the larger damping. This process is schematically illustrated in Fig. 4b and the following quantitative modeling verifies this mechanism.

Figure 4c plots the plasmon lifetime as a function of the plasmon frequency instead. The plasmon lifetime in graphene ribbons on DLC can be modeled by  $\tau = [\Gamma_0 + a/W_e + \Gamma_{ep}]^{-1}$ , where  $\Gamma_{ep}$  is the additional damping due to optical phonons.  $\Gamma_{ep}$  can be calculated from the electron self-energy due to the interaction with the optical phonon<sup>40,42</sup>, albeit its effect is relatively small for our measured ribbons on DLC substrate. Lifetime modeling of the hybrid plasmon-phonon mode (i.e. peak 3) in the SiO<sub>2</sub> counterpart is more involved, and we defer the details of the calculation to the Supplementary Information. After accounting for the plasmon decay channel via optical phonons, good agreement is achieved for plasmon lifetimes on both DLC and SiO<sub>2</sub>, as shown in Fig. 4c. Here, we emphasize an important observation regarding the latter. In SiO<sub>2</sub>, the hybrid mode begins with a long lifetime in the vicinity of the SP phonon energy at 1168 cm<sup>-1</sup>, but deteriorates rapidly to 20 femto seconds as its plasmon energy exceeds the optical phonon energy. This observation clearly highlights the important role of the various phonons on the plasmon lifetime.

Lastly, we strengthen our case for the plasmon decay via optical phonons by studying the carrier density dependence of the plasmon linewidth. Figure 4d shows the extinction spectra of ribbons array with a width of 100 nm on SiO<sub>2</sub>, at 4 different doping concentrations. The procedures for adjusting the doping concentration are described in the Methods section. We observed the increase of plasmon resonance frequency and amplitude with doping concentration, as expected from previously determined carrier density scaling law for plasmons in graphene<sup>4</sup>. As the plasmon frequency exceeds the graphene optical phonon energy, we observed a substantial increase in its resonance

linewidth as presented in the inset of Fig. 4d. On the contrary, plasmon resonance linewidth decreases with increasing doping in the far-infrared regime for graphene microstructures<sup>8</sup>. This observation further reinforces our picture of the plasmon decay channel via optical phonon emission.

### **Outlook of the graphene plasmonics**

Through the scaling of plasmonic structures into the nanometer regime, we unravel the importance of both substrate and intrinsic optical phonons on the plasmon dispersion and lifetimes. These new findings have important implications to further our understanding of basic electronic properties such as carrier screening, scattering and energy dissipation<sup>23,24,37,38,43</sup>. Most importantly, our study provides important guidelines for future graphene-based plasmonic devices. Indeed, interaction with optical phonons in graphene limits the quality factor of the plasmon resonance beyond the optical phonon frequency. As a result, the optimal operation wavelength of future graphene plasmonic devices should lie between the sub-terahertz and 6.5  $\mu\text{m}$ . Nevertheless, the hybridized plasmon-phonon mode in the vicinity of the surface polar phonon frequency features a long lifetime. It might be promising to exploit this for high performance mid-IR photonic devices.

### **Methods**

Large-scale graphene was grown using chemical vapor-phase deposition (CVD) on copper foil and then was transferred to  $\text{SiO}_2/\text{Silicon}$  or  $\text{DLC}/\text{Silicon}$  substrates<sup>15</sup>, before the subsequent e-beam lithography and oxygen plasma etching. The fabricated

nanoribbon arrays are designed to have width  $W$  equal to the spacing between the adjacent ribbons, corresponding to a filling factor of 50%. The array size is  $70\text{ }\mu\text{m}$  by  $70\text{ }\mu\text{m}$ , significantly larger than the infrared beam size ( $\sim 25\text{ }\mu\text{m}$  in diameter) used in the experiments. The as-prepared samples are hole-doped with a Fermi level of around  $-0.3\text{ eV}$ . By exposing the samples to nitric acid vapor for 10 minutes, the Fermi level can be further decreased to below  $-0.5\text{ eV}$ . Baking the doped sample at  $170\text{ }^{\circ}\text{C}$  can reduce the doping significantly. As a result, by adjusting the doping and baking time durations, we can achieve various doping concentrations, which can be determined using the extinction spectra in the far-infrared<sup>18</sup>. In the transmission measurements, we first recorded the transmission spectrum  $T_{per}$  for the perpendicularly polarized light with respect to the ribbons, and the extinction spectra for this particular polarization ( $1-T_{per}/T_0$ ) is obtained using the transmission of the bare substrate (with oxide but no graphene ribbons)  $T_0$  as the reference. The extinction spectrum ( $1-T_{//}/T_0$ ) for the light with polarization parallel to the nanoribbons was obtained in a similar manner. Light transmission through the substrate without graphene  $T_0$  has no polarization dependence. As shown in Fig. 1c, the extinction spectrum for parallel light polarization ( $1-T_{//}/T_0$ ) was close to zero in the entire wavelength of interest. Consequently, we used  $1-T_{per}/T_{//}$  for the extinction spectrum of the light with perpendicular polarization for simplicity, since in this case no reference point is necessary.

## Acknowledgments

The authors are grateful to B. Ek, J. Bucchignano, and S. (Jay) Chey for technical assistance and to V. Perebeinos, Z. Li of National High Magnetic Field Laboratory and

Prof. T. F. Heinz of Columbia University for stimulating discussions. F. X. acknowledges Prof. C. Gmachl of Princeton University and Dr. Y. Yao of Harvard University for help in the planning stage of the project. T. L. and F. G. acknowledge hospitality of KITP, supported in part by the NSF grant no. NSF PHY11-25915. T. L. also acknowledges partial support from NRI-INDEX and F.G. is also supported by the Spanish MICINN (FIS2008-00124, CONSOLIDER CSD2007-00010) and ERC grant 290846.

### **Author contributions**

F.X. and H.Y. initiated the project and conceived the experiments. W.Z., Y.W., H.Y. and F.X. fabricated the devices. H.Y. performed the measurements and data analysis. T.L. and F.G. provided modeling and theoretical foundation. M.F. participated in setting up the experimental apparatus. X.L. grew the CVD graphene. H.Y. and T. L. co-wrote the manuscript with inputs from F.X., and P.A. provided suggestions throughout the project. All authors commented on the manuscript.

### **Additional information**

Supplementary information accompanies this paper at [www.nature.com](http://www.nature.com). Reprints and permission information is available online at <http://npg.nature.com/reprintsandpermissions/>. Correspondence and requests for materials should be addressed to H.Y. ([hyan@us.ibm.com](mailto:hyan@us.ibm.com)), P.A. ([avouris@us.ibm.com](mailto:avouris@us.ibm.com)), and F.X. ([fxia@us.ibm.com](mailto:fxia@us.ibm.com)).

## Figure captions

### Figure 1. Schematics of the experiment

(a) Mid-IR transmission measurement scheme of graphene nanoribbons. The excitation light is broadband. False colors are used for the excitation light (rainbow) and the on-resonance light in graphene nanoribbons (red). (b) A scanning electron micrograph of a typical array of graphene nanoribbons. The width of the ribbon is around 100 nanometers. (c) The extinction spectra of a ribbon array on SiO<sub>2</sub> with the incident light polarization perpendicular (red) and parallel (grey) to the ribbons respectively. A weak 2<sup>nd</sup> order mode is indicated.

### Figure 2. Plasmons in graphene nanoribbons on diamond-like-carbon (DLC)

(a) The extinction spectra ( $1-T_{per}/T_{||}$ ) of graphene ribbons on DLC with different ribbon widths. The spectra were referenced using transmission of light with parallel polarization ( $T_{||}$ ). Inset: The plasmon resonance frequency as a function of the wave vector  $q = \pi/W$ , where  $W$  is the width of the nanoribbon. Red curve is a fit according to  $\omega_{pl} \sim \sqrt{q}$ . (b) The same data (red dots) as in (a), plotted as a function of wave vector  $q = \pi/W_e$ , where  $W_e = W - W_0$  is the effective ribbon width and  $W_0$  of 28 nm is used. The data from a lower Fermi level case is also plotted (grey dots). Dashed curves are fits based on the  $\sqrt{q}$  scaling. The shaded area is the intraband Landau damping region. The short bold black line just below 1600 cm<sup>-1</sup> indicates the graphene intrinsic optical phonon frequency.

### Figure 3. Plasmons in graphene nanoribbons on SiO<sub>2</sub>

(a) The extinction spectra ( $1-T_{per}/T_{||}$ ) of graphene ribbons on SiO<sub>2</sub> with different ribbon widths. The spectra are vertically displaced for clarity. The vertical dash line indicates the graphene optical phonon frequency. (b) Plasmon frequency as a function of the wave-vector  $q$  ( $= \pi/W_e$ ) for peaks 1, 2, 3, and a 2<sup>nd</sup> order dipolar mode peak in (a). The calculated loss function is plotted as a 2-dimensional pseudo-color background. The dashed line represents the plasmon frequency without considering the plasmon-phonon hybridization. Two surface polar phonons and the intrinsic optical phonon frequencies are indicated. See Supplementary Information for details of modeling.

### Figure 4. Origins of the plasmon damping

(a) The damping rates of the plasmons of graphene ribbons on DLC (red) and SiO<sub>2</sub> (grey) as a function of the effective width  $W_e$ . The data points are obtained from the linewidths of the spectra in Fig. 2a and Fig. 3a. For ribbons on SiO<sub>2</sub>, peak 3 is used. The red dashed curve is a fitted curve based on the model described in the main text and the grey dashed curve is a guide to the eye using  $\Gamma_p \propto (W - W_0)^{-x}$ . The data points for ribbons on SiO<sub>2</sub> with resonance frequency above the optical phonon frequency are indicated by the yellow rectangle. (b) An illustration of the plasmon damping process through the emission of an optical phonon together with the creation of an electron-hole pair. Interband and intraband damping regions are indicated. (c) The plasmon lifetimes of ribbons on DLC (red dots) and SiO<sub>2</sub> (grey dots) as the functions of the plasmon resonance frequencies. Dashed curves are calculated results, with the orange curve representing the contribution

from plasmon damping via phonon emission, the blue curve for contributions from both phonon emission and bulk scattering, and the grey (for SiO<sub>2</sub>) and red (for DLC) curves for contributions from phonon emission, bulk scattering and edge scattering. See Supplementary Information for details of calculation. The yellow region represents the frequency range larger than the graphene optical phonon frequency. (d) The extinction spectra of a ribbon with  $W$  of 100 nm on SiO<sub>2</sub> at four different doping levels. The inset shows the extracted full width at half maximum (FWHM) as a function of the corresponding plasmon resonance frequency.

## References

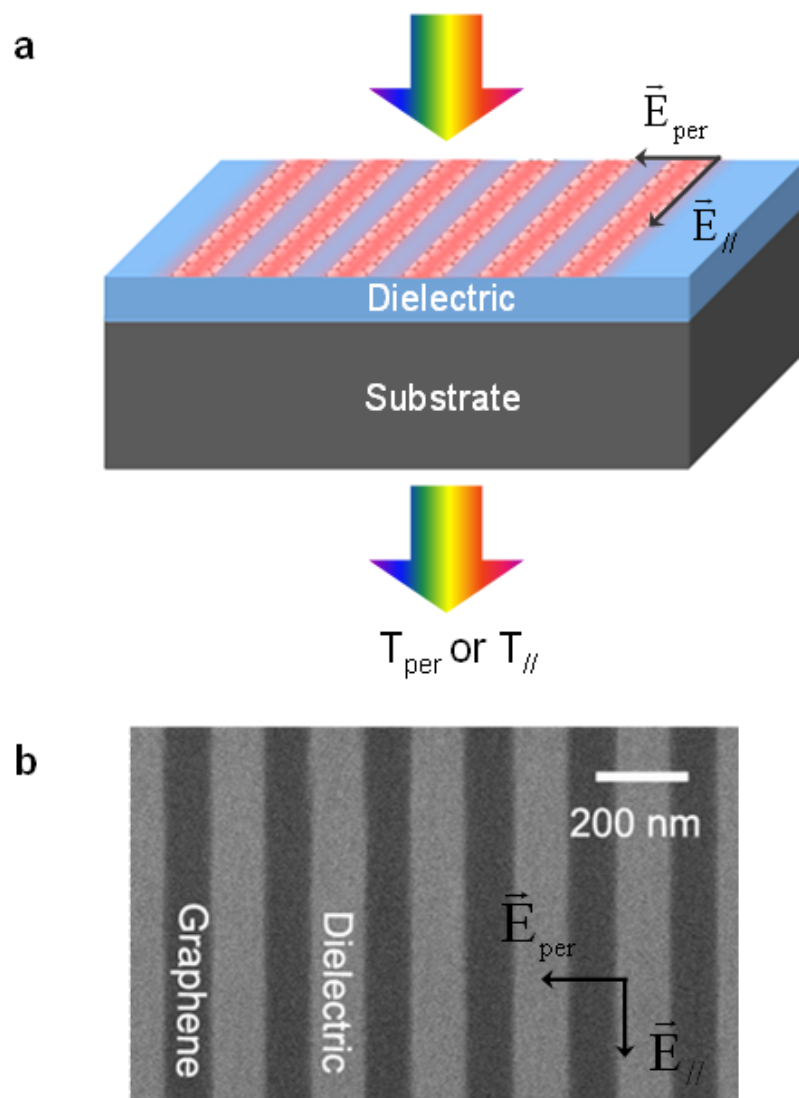
1. Maier, S., *Plasmonics: Fundamentals and Applications* 1st edn (Springer, New York, 2007).
2. Koppens, F. H. L., Chang, D. E. & Javier Garcia de Abajo, F. Graphene plasmonics: A platform for strong light-matter interactions. *Nano Lett.* **11**, 3370–3377 (2011).
3. Vakil, A. & Engheta, N. Transformation optics using graphene. *Science* **332**, 1291–1294 (2011).
4. Ju, L. *et al.* Graphene plasmonics for tunable terahertz metamaterials. *Nature Nanotech.* **6**, 630–634 (2011).
5. Fei, Z. *et al.* Infrared nanoscopy of Dirac plasmons at the graphene/SiO<sub>2</sub> interface. *Nano Lett.* **11**, 4701–4705 (2011).
6. Fei, Z. *et al.* Gate-tuning of graphene plasmons revealed by infrared nano-imaging. *Nature*, doi:10.1038/nature11253 (2012).
7. Chen, J. *et al.* Optical nano-imaging of gate-tunable graphene plasmons. *Nature*, doi:10.1038/nature11254 (2012).
8. Yan, H. *et al.* Tunable infrared plasmonic devices using graphene/insulator stacks. *Nature Nanotech.* **7**, 330–334 (2012).
9. Yan, H. *et al.* Infrared spectroscopy of tunable Dirac terahertz magneto-plasmons in graphene. *Nano Lett.* **12**, 3766–3771 (2012).
10. Han, M. Y., Ozyilmaz, B., Zhang, Y. & Kim, P. Energy band-gap engineering of graphene nanoribbons. *Phys. Rev. Lett.* **98**, 206805 (2007).
11. Berger, C. *et al.* Electronic confinement and coherence in patterned epitaxial graphene. *Science* **312**, 1191–1196 (2006).
12. Todd, K., Chou, H. T., Amasha, S. & Goldhaber-Gordon, D. Quantum dot behavior in graphene nanoconstrictions. *Nano Lett.* **9**, 416–421 (2008).
13. Kreibig, U. & Vollmer, M. *Optical Properties of Metal Clusters* 1st edn (Springer, Berlin, 1995).
14. Link, S. & El-Sayed, M. A. Size and temperature dependence of the plasmon absorption of colloidal gold nanoparticles. *J. Phys. Chem. B* **103**, 4212–4217 (1999).
15. Li, X. *et al.* Large-area synthesis of high-quality and uniform graphene films on copper foils. *Science* **324**, 1312–1314 (2009).

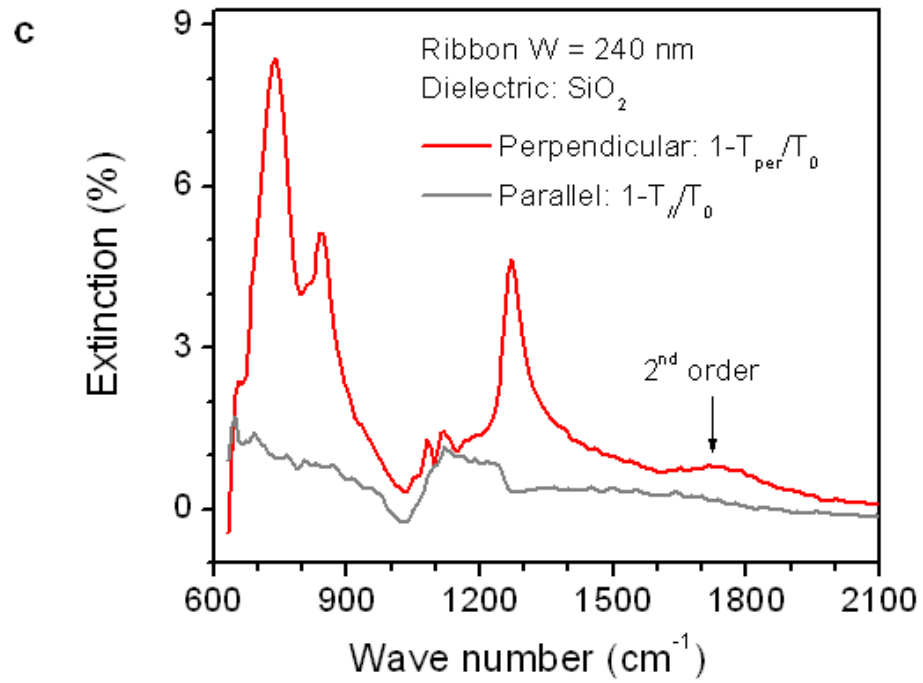


16. Wu, Y. *et al.* High-frequency, scaled graphene transistors on diamond-like carbon. *Nature* **472**, 74–78 (2011).
17. Kucírková, A. & Navrátil, K. Interpretation of infrared transmittance spectra of SiO<sub>2</sub> thin films. *Appl. Spectrosc.* **48**, 113–120 (1994).
18. Yan, H. *et al.* Infrared spectroscopy of wafer-scale graphene. *ACS Nano* **5**, 9854–9860 (2011).
19. Fuchs, R. & Kliever, K. L. Optical modes of vibration in an ionic crystal slab. *Phys. Rev.* **140**, A2076–A2088 (1965).
20. Dubois, L. H. & Schwartz, G. P. Surface optical phonons and hydrogen chemisorption on polar and nonpolar faces of GaAs, InP, and GaP. *Phys. Rev. B* **26**, 794–802 (1982).
21. Matz, R. & Luth, H. Conduction-band surface plasmons in the electron-energy-loss spectrum of GaAs(110). *Phys. Rev. Lett.* **46**, 500–503 (1981).
22. Wang, S. Q. & Mahan, G. D. Electron scattering from surface excitations. *Phys. Rev. B* **6**, 4517–4524 (1972).
23. Fratini, S. & Guinea, F. Substrate-limited electron dynamics in graphene. *Phys. Rev. B* **77**, 195415 (2008).
24. Hwang, E. H., Sensarma, R. & Das Sarma, S. Plasmon-phonon coupling in graphene. *Phys. Rev. B* **82**, 195406 (2010).
25. Liu, Y. & Willis, R. F. Plasmon-phonon strongly coupled mode in epitaxial graphene. *Phys. Rev. B* **81**, 081406 (2010).
26. Stern, F. Polarizability of a two-dimensional electron gas. *Phys. Rev. Lett.* **18**, 546–548 (1967).
27. Wunsch, B., Stauber, T. & Guinea, F. Dynamical polarization of graphene at finite doping. *New J. Phys.* **8**, 318 (2006).
28. Hwang, E. H. & Das Sarma, S. Dielectric function, screening, and plasmons in two-dimensional graphene. *Phys. Rev. B* **75**, 205418 (2007).
29. Mikhailov, S. A. & Savostianova, N. A. Microwave response of a two-dimensional electron stripe. *Phys. Rev. B* **71**, 035320 (2005).
30. Thongrattanasiri, S., Manjavacas, A. & Garcia de Abajo, F. J. Quantum finite-size effects in graphene plasmons. *ACS Nano* **6**, 1766–1775 (2012).
31. Radovic, L. R. & Bockrath, B. On the chemical nature of graphene edges: origin of stability and potential for magnetism in carbon materials. *J. Am. Chem. Soc.* **127**, 5917–5927 (2005).
32. Areshkin, D. A., Gunlycke, D. & White, C. T. Ballistic transport in graphene nanostrips in the presence of disorder: importance of edge effects. *Nano Lett.* **7**, 204–210 (2006).
33. Fano, U. Effects of configuration interaction on intensities and phase shifts. *Phys. Rev.* **124**, 1866–1878 (1961).
34. Jablan, M., Soljacic, M. & Buljan, H. Unconventional plasmon-phonon coupling in graphene. *Phys. Rev. B* **83**, 161409 (2011).
35. Mahan, G. D. *Many-Particle Physics* 3rd edn (Kluwer Academic/Plenum, New York, 2000).
36. Ferrari, A. C. *et al.* Raman spectrum of graphene and graphene layers. *Phys. Rev. Lett.* **97**, 187401 (2006).

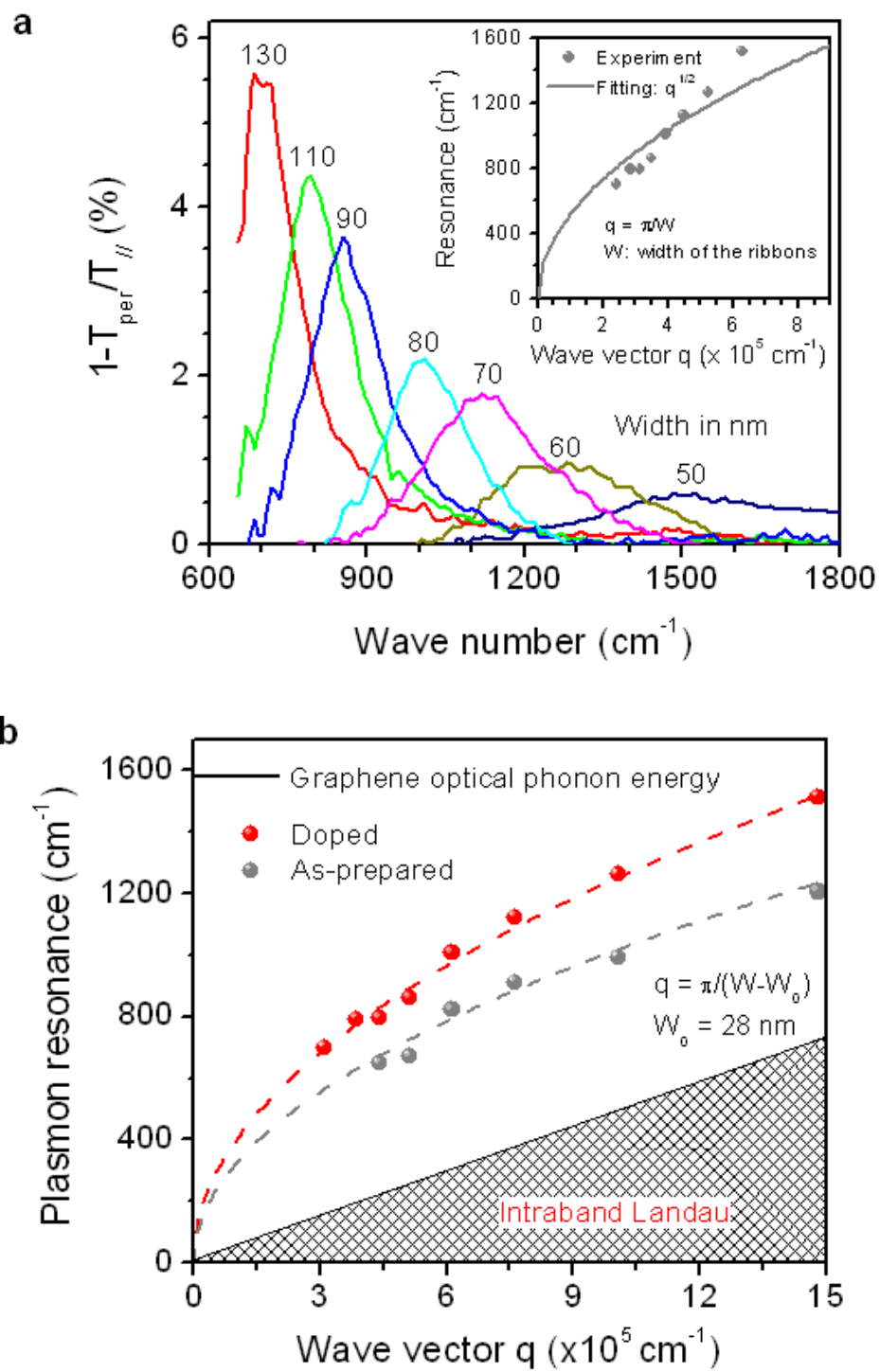
37. Perebeinos, V. & Avouris, Ph. Inelastic scattering and current saturation in graphene. *Phys. Rev. B* **81**, 195442 (2010).
38. Fischetti, M. V., Neumayer, D. A. & Cartier, E. A. Effective electron mobility in Si inversion layers in metal--oxide--semiconductor systems with a high-kappa insulator: The role of remote phonon scattering. *J. Appl. Phys.* **90**, 4587-4608 (2001).
39. Adato, R. *et al.* Radiative engineering of plasmon lifetimes in embedded nanoantenna arrays. *Opt. Expr.* **18**, 4526-4537 (2010).
40. Jablan, M., Buljan, H. & Soljagic, M. Plasmonics in graphene at infrared frequencies. *Phys. Rev. B* **80**, 245435 (2009).
41. Hillenbrand, R., Taubner, T. & Keilmann, F. Phonon-enhanced light-matter interaction at the nanometre scale. *Nature* **418**, 159-162 (2002).
42. Park, C.-H., Giustino, F., Cohen, M. L. & Louie, S. G. Velocity renormalization and carrier lifetime in graphene from the electron-phonon interaction. *Phys. Rev. Lett.* **99**, 086804 (2007).
43. Low, T. *et al.* Cooling of photoexcited carriers in graphene by internal and substrate phonons. *Phys. Rev. B* **86**, 045413 (2012).

**Figure 1 Schematics of the experiment**

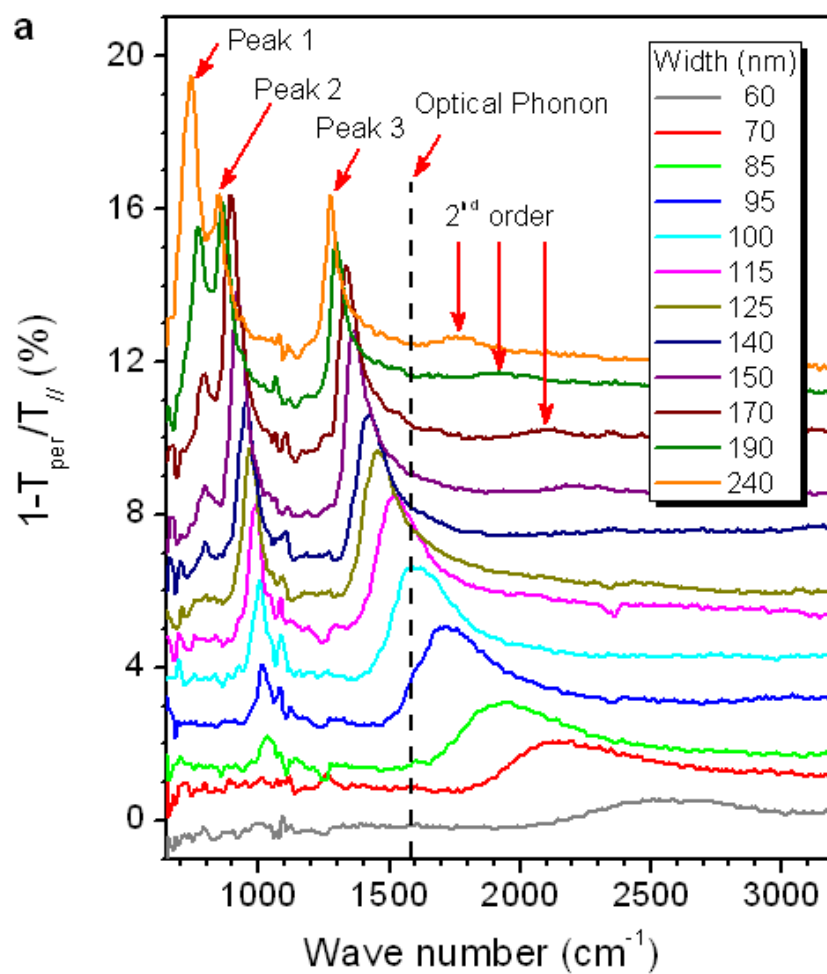


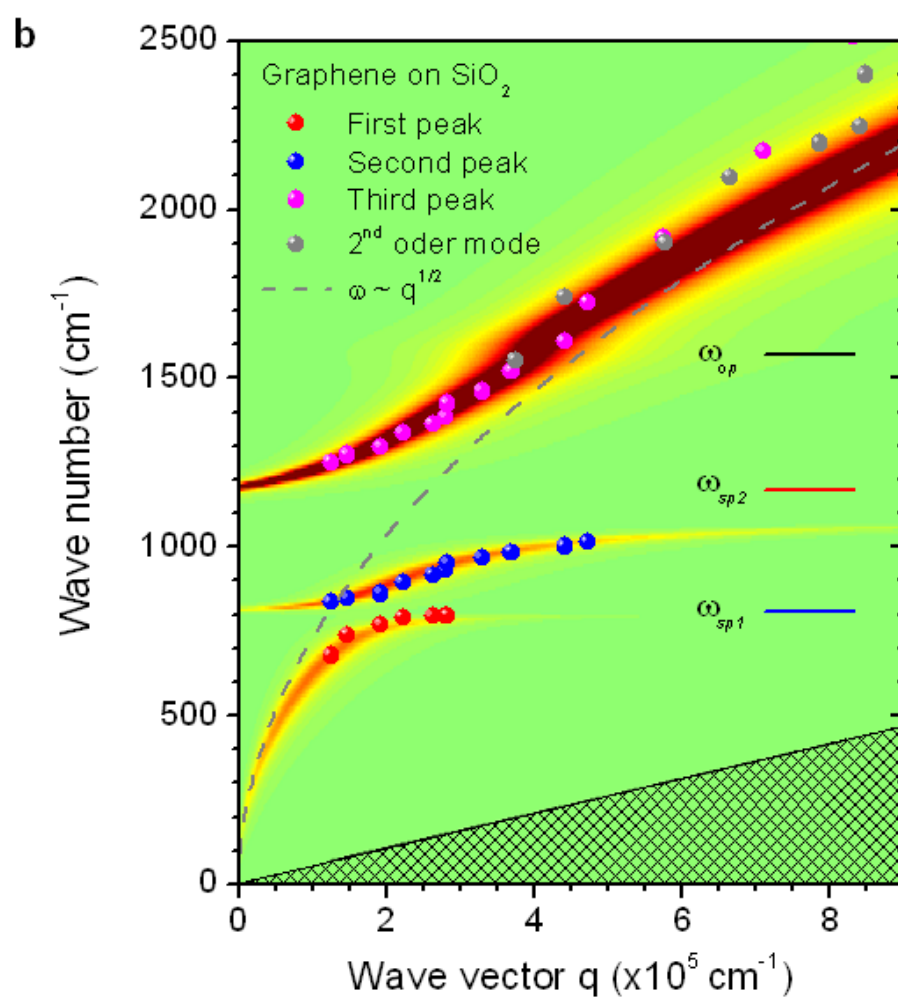


**Figure 2 Graphene nanoribbons on diamond-like-carbon (DLC)**

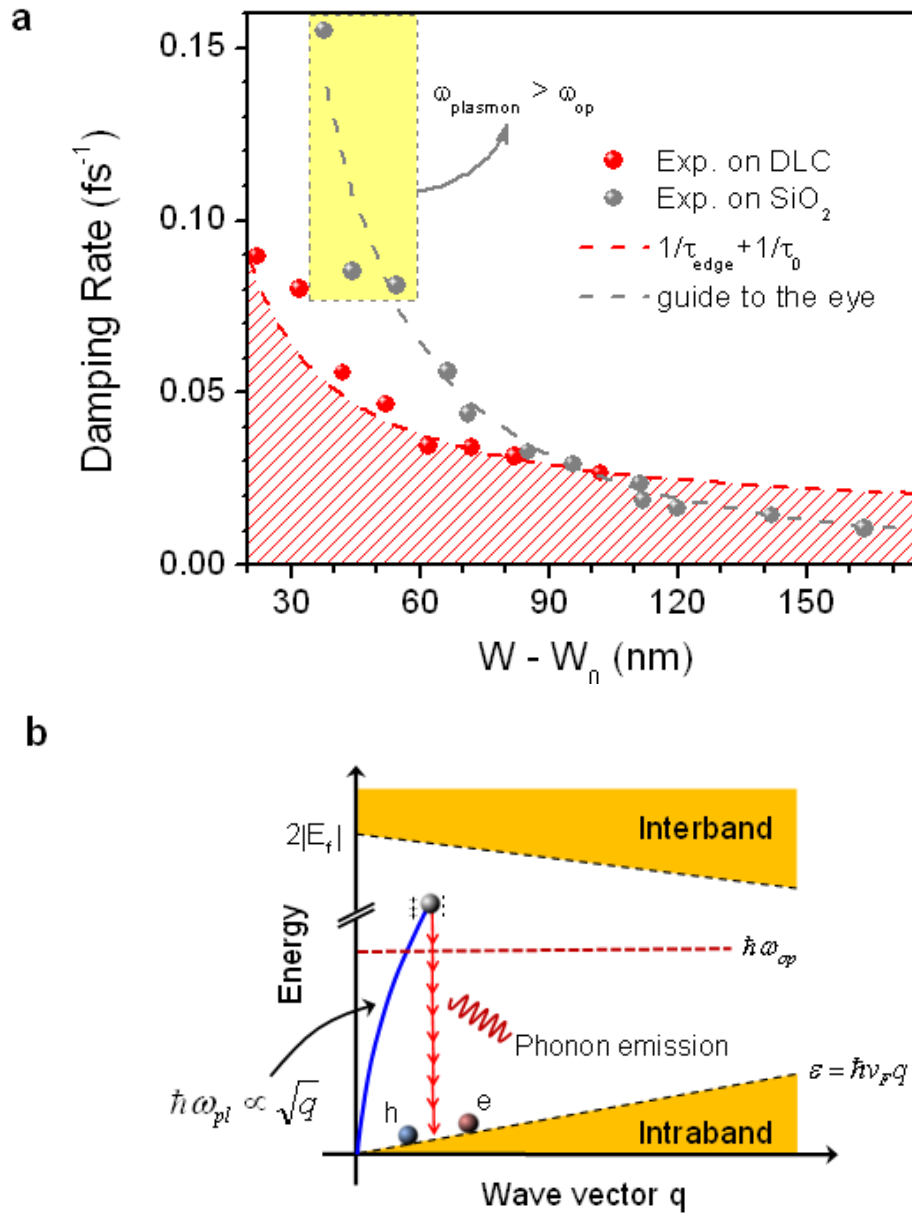


**Figure 3 Graphene nanoribbons on Silicon Dioxide (SiO<sub>2</sub>)**

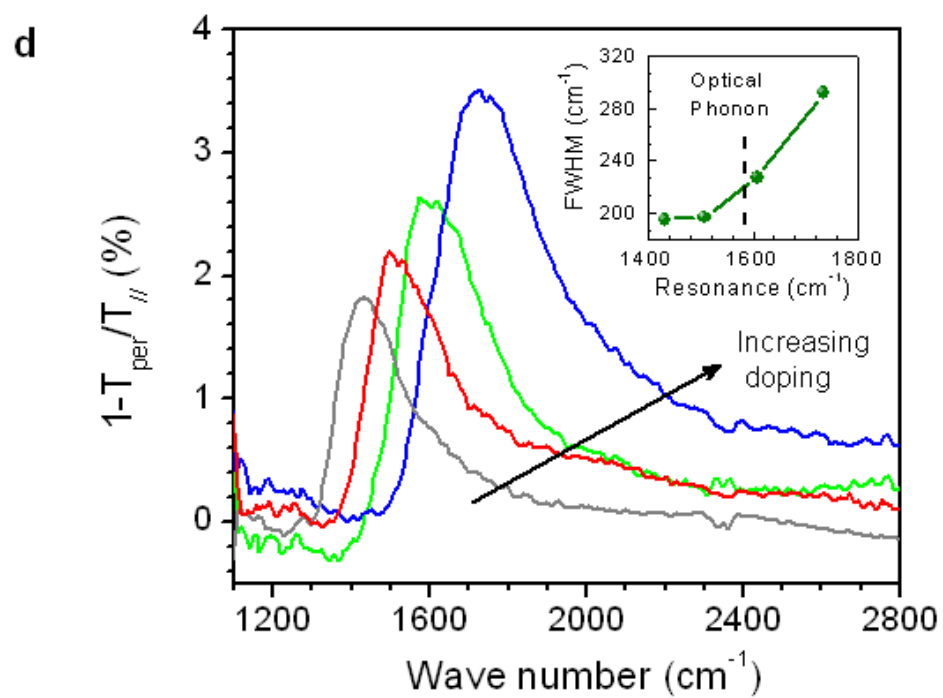
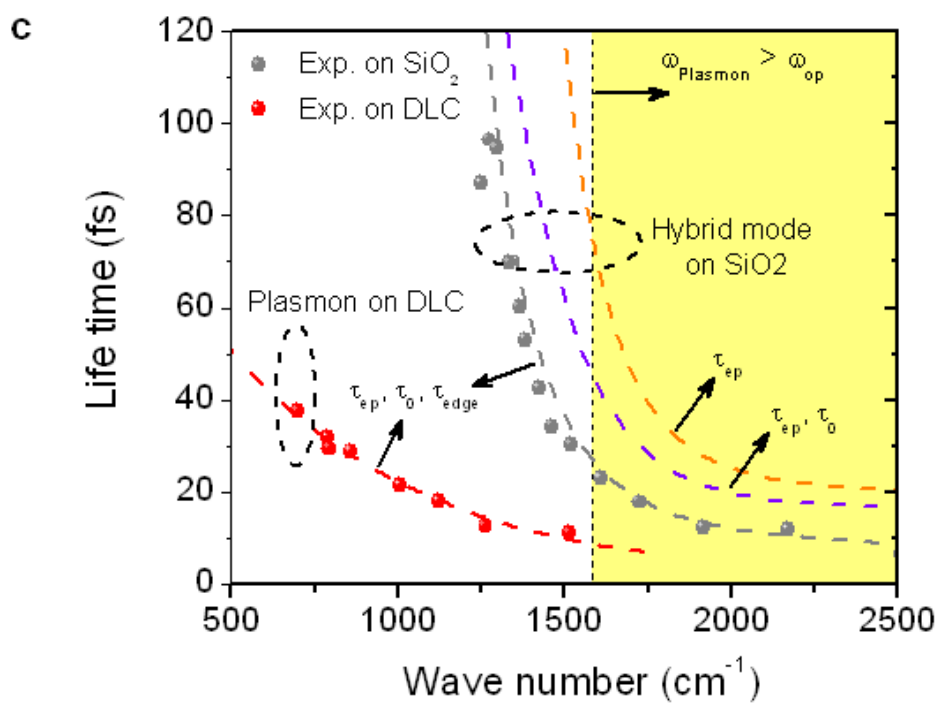




**Figure 4 Origins of the plasmon damping**







**Supplementary Information:**  
**Mid-infrared plasmons in scaled graphene nanostructures**

Hugen Yan<sup>1†</sup>, Tony Low<sup>1†</sup>, Wenjuan Zhu<sup>1</sup>, Yanqing Wu<sup>1</sup>, Marcus Freitag<sup>1</sup>,  
Xuesong Li<sup>1</sup>, Francisco Guinea<sup>2</sup>, Phaedon Avouris<sup>1</sup> and Fengnian Xia<sup>1</sup>

<sup>1</sup> *IBM T.J. Watson Research Center,  
Yorktown Heights, NY 10598, USA*

<sup>2</sup> *Instituto de Ciencia de Materiales de Madrid. CSIC.  
Sor Juana Inés de la Cruz 3. 28049 Madrid, Spain*

<sup>†</sup>*These authors contributed equally to this work*

## I. CALCULATING THE RPA DIELECTRIC FUNCTION AND LOSS FUNCTION

This section describes the modeling of the loss function in graphene on SiO<sub>2</sub> as shown in the intensity plot of Fig. 3b in the main manuscript.

### A. Intrinsic phonons

The only intrinsic phonons with momenta and energies similar to the graphene plasmons in our experiment are the longitudinal/transverse optical (LO/TO) phonons near the  $\Gamma$  point, with energies  $\hbar\omega_{op} \approx 0.2$  eV. On symmetry grounds[1], their coupling to electrons can be written as[2, 3]

$$\mathcal{H}_{e-op}(\mathbf{r}) = g_0 \begin{pmatrix} 0 & u_y(\mathbf{r}) + iu_x(\mathbf{r}) \\ u_y(\mathbf{r}) - iu_x(\mathbf{r}) & 0 \end{pmatrix} = \frac{g_0}{v_F} \hat{\mathbf{j}}(\mathbf{r}) \times \mathbf{u}(\mathbf{r}) \quad (1)$$

where  $v_F$  is the Fermi velocity and  $g_0$  the coupling constant. The coupling constant can be estimated from the change with bond length of the hopping between nearest neighbor carbon  $\pi$  orbitals[4, 5],  $g_0 \approx \partial t / \partial l$ . The electronic Hamiltonian is described within each valley (and spin) in terms of the amplitudes on A/B sublattices,  $\hat{\mathbf{j}}(\mathbf{r})$  is the single-particle current operator and  $\mathbf{u}(\mathbf{r})$  is the relative displacement of the two sublattices. Their representation in terms of electron and phonon ladder operators, i.e.  $\hat{a}_{\mathbf{k}}$  and  $\hat{b}_{\mathbf{q}}$  respectively, are given by,

$$\hat{\mathbf{j}}(\mathbf{r}) = \frac{1}{A} \sum_{\mathbf{kq}} v_F \hat{a}_{\mathbf{k}}^\dagger \hat{\sigma} \hat{a}_{\mathbf{k+q}} e^{i\mathbf{q} \cdot \mathbf{r}} \equiv \frac{1}{A} \sum_{\mathbf{q}} \hat{\mathbf{j}}_{\mathbf{q}} e^{i\mathbf{q} \cdot \mathbf{r}} \quad (2)$$

$$\mathbf{u}(\mathbf{r}) = \sqrt{\frac{\hbar}{2\rho_m A \omega_{op}}} \sum_{\mathbf{q}\lambda} (\hat{b}_{\mathbf{q}\lambda} + \hat{b}_{-\mathbf{q}\lambda}^\dagger) \mathbf{e}_{\mathbf{q}\lambda} e^{i\mathbf{q} \cdot \mathbf{r}} \quad (3)$$

where  $\hat{\sigma}$  are the Pauli spin matrices and  $\mathbf{e}_{\mathbf{q}\lambda}$  are the polarization vectors.  $\lambda$  denotes the phonon modes,  $\rho_m$  is the mass density of graphene and  $A$  is its area. Using standard perturbation techniques, the effective electron-electron interaction mediated by optical phonons can be written as,

$$\mathcal{V}_{el-el}^{op} = \frac{1}{A^2} \sum_{\mathbf{q}\lambda} \frac{1}{v_F^2} |M_{op}|^2 \mathcal{D}_\lambda^0(\omega) \hat{\mathbf{j}}_{\mathbf{q}} \cdot \hat{\mathbf{j}}_{-\mathbf{q}} \equiv \frac{1}{A^2} \sum_{\mathbf{q}\lambda} v_{op,\lambda} \hat{\mathbf{j}}_{\mathbf{q}} \cdot \hat{\mathbf{j}}_{-\mathbf{q}} \quad (4)$$

where the scattering matrix elements and the free phonon Green's function are

$$|M_{op}|^2 = \frac{\hbar g_0^2}{2\rho_m \omega_{op}} \quad , \quad \mathcal{D}_\lambda^0(\omega) = \frac{2\omega_{op}}{\hbar((\omega + i\hbar/\tau_{op})^2 - \omega_{op}^2)} \quad (5)$$

where  $\tau_{op}$  phenomenologically describes the phonon lifetime.

## B. Surface polar phonons

Polar substrates, such as SiO<sub>2</sub> and BN have optical piezoelectric modes at energies  $\hbar\omega_{sp}$ . These modes induce electric fields which couple to the carriers in graphene[6, 7]. At long wavelengths, the effect of these can be described in terms of the dielectric function of the substrate,

$$\mathcal{H}_{e-sp} = \frac{1}{A} \sum_{\mathbf{k}\mathbf{q}} M_{sp} \hat{a}_{\mathbf{k}+\mathbf{q}}^\dagger \hat{a}_{\mathbf{k}} (\hat{b}_{\mathbf{q}\lambda} + \hat{b}_{-\mathbf{q}\lambda}^\dagger) \quad (6)$$

with the scattering matrix elements defined as,

$$|M_{sp}|^2 = \frac{\pi e^2}{\epsilon_0} \frac{e^{-2qz_0}}{q} \mathcal{F}^2, \quad \mathcal{F}^2 = \frac{\hbar\omega_{sp}}{2\pi} \left( \frac{1}{\epsilon_{high} + \epsilon_{env}} - \frac{1}{\epsilon_{low} + \epsilon_{env}} \right) \quad (7)$$

where  $z_0$  is the graphene-substrate separation,  $\mathcal{F}^2$  describes the Fröhlich coupling strength,  $\epsilon_{low}$  ( $\epsilon_{high}$ ) are the low (high) frequency dielectric constant of the dielectric and  $\epsilon_{env}$  is that of the environment. The effective electron-electron interaction mediated by surface optical phonons calculated from standard perturbation techniques yields[8],

$$\mathcal{V}_{el-el}^{sp} = \frac{1}{A^2} \sum_{\mathbf{q}\lambda} |M_{sp}|^2 \mathcal{D}_\lambda^0(\omega) \hat{\rho}_{\mathbf{q}} \hat{\rho}_{-\mathbf{q}} \equiv \frac{1}{A^2} \sum_{\mathbf{q}\lambda} v_{sp,\lambda} \hat{\rho}_{\mathbf{q}} \hat{\rho}_{-\mathbf{q}} \quad (8)$$

where  $\hat{\rho}_{\mathbf{q}} \equiv \sum_{\mathbf{k}} \hat{a}_{\mathbf{k}}^\dagger \hat{a}_{\mathbf{k}+\mathbf{q}}$  and  $\mathcal{D}_\lambda^0(\omega)$  contains also a phenomenological phonon lifetime of  $\tau_{sp}$ .

## C. Dielectric response

The plasmon response of graphene begins with finding the dielectric function. A satisfactory approximation can be obtained by adding the separate contributions *independently*. An effective interaction between electrons is given by the sum of the direct Coulomb interaction  $v_c(q) = e^2/2q\epsilon_0$  and the two electrons interaction mediated by surface phonon  $v_{sp,\lambda}(q, \omega)$ . The RPA expansion of the dielectric function,  $\epsilon_T^{rpa}(q, \omega)$ , can be expressed with this effective interaction[9, 10]

$$v_{eff}(q, \omega) = \frac{v_c(q)}{\epsilon_T^{rpa}(q, \omega)} = \frac{v_c(q) + \sum_{\lambda} v_{sp,\lambda}}{1 - [v_c(q) + \sum_{\lambda} v_{sp,\lambda}] \Pi_{\rho,\rho}^0(q, \omega)} \quad (9)$$

where  $\Pi_{\rho,\rho}^0(q, \omega)$  is the non-interacting part (i.e. the pair bubble diagram) of the charge-charge correlation function given by a modified Lindhard function[11, 12],

$$\Pi_{\rho,\rho}^0(q, \omega) = -\frac{g_s}{(2\pi)^2} \sum_{nn'} \int_{\text{BZ}} d\mathbf{k} \frac{n_F(\xi_{\mathbf{k}}) - n_F(\xi_{\mathbf{k}+\mathbf{q}})}{\xi_{\mathbf{k}} - \xi_{\mathbf{k}+\mathbf{q}} + \hbar\omega + i\hbar/\tau_e} F_{nn'}(\mathbf{k}, \mathbf{q}) \quad (10)$$

where  $n_F(\xi_{\mathbf{k}})$  is the Fermi-Dirac distribution function,  $F_{nn'}(\mathbf{k}, \mathbf{q})$  is the band overlap function of Dirac spectrum and  $\tau_e$  is the lifetime of electrons. While the polar surface phonons couple to the charge density operator, the intrinsic optical phonon couple instead to the current operator. Its contribution to the dielectric function is given by  $v_{op}(q, \omega)\Pi_{j,j}^0(q, \omega)$ , where  $\Pi_{j,j}^0(q, \omega)$  is the current-current correlation function. We note that from the usual charge continuity equation,  $i\partial_t\hat{\rho}_{\mathbf{q}} = \mathbf{q} \cdot \hat{\mathbf{j}}_{\mathbf{q}}$ , it follows that,

$$q^2\Pi_{j,j}(q, \omega) = \omega^2\Pi_{\rho,\rho}(q, \omega) - v_F \left\langle \left[ \mathbf{q} \cdot \hat{\mathbf{j}}_{\mathbf{q}}, \hat{\rho}_{-\mathbf{q}} \right] \right\rangle \quad (11)$$

where the second term in Eq. 11 is purely real and  $\propto q^2$  as calculated in Ref. [13]. The imaginary part of  $\Pi_{j,j}(q, \omega)$  can be obtained just from  $\Im[\frac{\omega^2}{q^2} \times \Pi_{\rho,\rho}(q, \omega)]$ . Collective modes with self consistent oscillations of the carrier charge can be obtained from the zeros of the full dielectric function

$$\epsilon_T^{rpa}(q, \omega) = \epsilon_{env} - v_c\Pi_{\rho,\rho}^0(q, \omega) - \epsilon_{env} \sum_{\lambda} v_{sp,\lambda}\Pi_{\rho,\rho}^0(q, \omega) - \epsilon_{env}v_{op}\Pi_{j,j}^0(q, \omega) \quad (12)$$

where  $\epsilon_{env}$  is the dielectric constant of graphene's environment.

#### D. Loss function

Our spectroscopy experiments measure the extinction spectra defined as  $Z \equiv -\delta T/T_0$  with  $\delta T = T - T_0$ , where  $T$  ( $T_0$ ) is the measured transmission with (without) plasmon excitations. In the experiment, a superlattice of graphene ribbons of width  $W$  defines the momentum i.e.  $q = \pi/(W - W_0)$ .  $W_0$  accounts for the difference between physical and electrical device's width. Varying the frequency of the incident light excitation,  $\omega$ , polarized perpendicularly (and parallely) to the ribbon, allows one to quantify the extinction spectra  $Z(q, \omega)$ , as first demonstrated in Ref. [14]. Resonance peaks in  $Z(q, \omega)$  corresponds to enhanced optical absorption by graphene originating from plasmon oscillations[14–16] and can best be described by,

$$Z(q, \omega) \sim -\Im \left[ \frac{1}{\epsilon_T^{rpa}} \right] \quad (13)$$

where the latter is known as the loss function, which describes the ability of the system to dissipate energy via plasmon excitations and can be calculated from Eq. 12.

Using the above theory, we plot the loss function in graphene on SiO<sub>2</sub> as shown in Fig.3b of the main manuscript. The calculations include interactions with the intrinsic and SiO<sub>2</sub> substrate phonons. Graphene doping is assumed to be  $E_f = -0.43$  eV and an effective  $\epsilon_{env} = 1.5$ . The frequencies of the various phonon modes are assumed to be at  $\omega_{op} = 1580$  cm<sup>-1</sup>,  $\omega_{sp1} = 806$  cm<sup>-1</sup> and  $\omega_{sp2} = 1168$  cm<sup>-1</sup>. The damping time used in those plots are  $\tau_e = 0.1$  ps,  $\tau_{op} = 70$  fs and  $\tau_{sp} = 1$  ps. The coupling parameters used are  $g_0 = 7.7$  eV Å<sup>-1</sup>,  $\mathcal{F}_{sp1}^2 = 0.2$  meV and  $\mathcal{F}_{sp2}^2 = 2$  meV. Note that another substrate phonon at  $\omega_{op} = 460$  cm<sup>-1</sup> was not included in the calculation, given that our experiment data are far above that frequency.

## II. CALCULATING LIFETIMES OF THE PLASMON AND COUPLED PLASMON-PHONON MODES

This section describes the modeling of the plasmon lifetime in graphene on DLC and SiO<sub>2</sub> as shown in Fig. 4a and 4c of the main manuscript.

In the above previous analysis, the damping mechanisms for the plasmons are not discussed. Exchange of energy and momentum during scattering of plasmons can bring it into the Landau damping regime, leading to finite damping. In fact, when the plasmon energy exceeds the optical phonon energy, it can decay into a phonon together with an electron-hole pair, in such a way that the total momentum is conserved. In a phenomenological way, this decay can be accounted for through the single particle excitations, which have a finite lifetime  $\tau_e$ , when their energies exceed the optical phonon energy[17], for example. Damping related to scattering with the ribbon's edges and a background damping due to impurities in the bulk can also be incorporated in  $\tau_e$ . Finite phonon lifetime,  $\tau_{sp}$ , can also influence to plasmon damping in the coupled plasmon-phonon modes. Below, we present our description of plasmon damping in the presence and absence of coupling with the surface phonon modes.

We are interested in the regime where  $\omega > v_F q$  and  $E_f \gg \hbar\omega$ . In this limit,

$$\Pi_{\rho,\rho}^0(q, \omega) \approx \frac{E_f q^2}{\pi \hbar^2 (\omega + i\delta_e)^2} \quad (14)$$

where  $\delta_e$  is the single-particle related damping in graphene defined as  $\delta_e \equiv 1/\tau_e$ . In the

absence of substrate phonon interactions, such as the case of graphene on a DLC substrate, the plasmon frequency is simply  $\omega = \omega_{pl} + i\delta_e$ , where  $\omega_{pl}^2 = q|E_f|e^2/2\pi\hbar^2\epsilon_0\epsilon_{env}$  and  $\delta_e$  also corresponds to plasmon damping. Note that in the regime we are considering i.e.  $\omega > v_F q$  and  $E_f \gg \hbar\omega$ , Landau damping is excluded. Guided by experiments, the plasmon hybridizes strongly with one of the surface phonon modes with  $\omega_{sp} \approx 0.145$  eV on SiO<sub>2</sub> substrate. For  $\omega > \omega_{sp}$ , we can write a simpler dielectric function,

$$\epsilon_T^{rpa} \approx \epsilon_{env} \left[ 1 - \frac{\omega_{pl}(q)^2}{(\omega + i\delta_e)^2} - \frac{\tilde{\omega}_{sp}^2}{(\omega + i\delta_{sp})^2 - \omega_{sp}^2 + \tilde{\omega}_{sp}^2} \right], \quad \tilde{\omega}_{sp} \equiv \sqrt{\frac{4\pi}{\hbar}\omega_{sp}\mathcal{F}^2} \quad (15)$$

where  $\delta_{sp}$  is the surface phonons damping rate defined as  $\delta_{sp} \equiv 1/\tau_{sp}$ . The frequencies of the coupled plasmon-phonon modes can be obtained by setting  $\epsilon_T^{rpa} = 0$  i.e.,

$$\omega^4 + i2\omega^3(\delta_{sp} + \delta_e) - \omega^2(\omega_{sp}^2 + \omega_{pl}(q)^2) - i2\omega(\omega_{sp}^2\delta_e + \omega_{pl}(q)^2\delta_{sp}) + \omega_{pl}(q)^2(\omega_{sp}^2 - \tilde{\omega}_{sp}^2) = 0 \quad (16)$$

which can be solved numerically. In the limit where  $\delta_e = \delta_{sp} = 0$ , it reduces to a simple biquadratic equation with coupled plasmon-phonon modes solutions given by,

$$\omega_{\pm}^2 = \frac{\omega_{pl}^2 + \omega_{sp}^2}{2} \pm \frac{\sqrt{(\omega_{pl}^2 + \omega_{sp}^2)^2 - 4\omega_{pl}^2(\omega_{sp}^2 - \tilde{\omega}_{sp}^2)}}{2} \quad (17)$$

In the general case where  $\delta_e = \delta_{ph} \neq 0$ , we solve for the coupled plasmon-phonon modes via Eq. 16 numerically. However, in the  $q = 0$  limit, it can be shown by setting  $\epsilon_T^{rpa} = 0$  in Eq. 15 that  $\omega = \omega_{sp} - i\delta_{sp}$ . Therefore, the lifetime of the plasmon with frequency in the vicinity of the surface phonon frequency is determined by the surface phonon lifetime instead.

In this work, we assume that  $\tau_{sp}$  is constant, to be fitted to experiment. Here, we discuss model description of the electron lifetime  $\tau_e$ . Including relevant scattering mechanisms in our experiments,  $\tau_e$  is given by,

$$\tau_e(q, \omega) \approx [\tau_0^{-1} + \tau_{edge}(q)^{-1} + \tau_{ep}(\omega)^{-1}]^{-1} \quad (18)$$

where  $\tau_0$  describes a background damping due to scattering with impurities and  $\tau_{edge}(q) \approx a/(W - W_0)^b$  is related to scattering off the ribbon edges.  $\tau_0 \approx 85$  fs as measured from the Drude response of large area, unpatterned graphene.  $a \approx 2 \times 10^6$ , of the order of Fermi velocity and  $b = 1$  as discussed in the main text.  $\tau_{ep}(\omega)$  is electron lifetime due to scattering

with optical phonons. It is related to the electron self-energy  $\Sigma_{ep}$  via  $\tau_{ep} = \hbar/2\Im[\Sigma_{ep}]$  given by[9],

$$\Sigma_{ep}(\omega) = -k_B T \sum_{\mathbf{q}, \omega_\lambda} |M_{op}|^2 \mathcal{D}_\lambda(\omega_\lambda)^0 \mathcal{G}^0(\mathbf{k}_f + \mathbf{q}, \omega + \omega_\lambda) \quad (19)$$

where  $\mathcal{G}^0$  is the electron Green function and  $\mathbf{k}_f$  is the Fermi wavevector. According to density functional calculations, the imaginary part of  $\Sigma_{ep}$  can be approximated by[18],

$$\Im[\Sigma_{ep}(\omega)] = \gamma_0 |\hbar\omega + \hbar\omega_0 + E_f| \times \frac{1}{2} \left[ \text{erf}\left(\frac{\hbar\omega - \hbar\omega_0}{\Delta_{ph}}\right) + \text{erf}\left(\frac{-\hbar\omega - \hbar\omega_0}{\Delta_{ph}}\right) + 2 \right] \quad (20)$$

where  $\gamma_0$  describes the effective e-ph coupling and  $\Delta_{ph}$  accounts for various energy broadening effects such as the deviation from the Einstein phonon dispersion model. They are estimated to be  $\gamma_0 \approx 0.018$  and  $\Delta_{ph} \approx 50$  meV from density function calculations[18].

As discussed previously, in the absence of interaction with the surface phonons, the plasmon lifetime is simply  $\tau_e(q, \omega = \omega_{pl})$ . In the presence of interaction with surface phonons, the plasmon lifetime for the plasmon-phonon coupled modes can be solved via Eq.16 numerically, with  $\delta_e \approx [\tau_e(q, \omega = \omega_{pl}(q))]^{-1}$ . The computed plasmon damping rates or lifetimes on DLC and SiO<sub>2</sub> substrates are shown in Fig.4a and 4c of the main manuscript. There, we assumed graphene doped at  $E_f \sim -0.43$  eV.

Previously, we also show in Fig. 3b of the main manuscript the RPA loss function in SiO<sub>2</sub>. However, the electron lifetime there was simply assumed to be constant. In Fig.S1, we calculate again the RPA loss function in SiO<sub>2</sub>, but this time including the electron damping  $\delta_e$  which describes our experiment as detailed in this section. After the inclusion of a more accurate description of electron damping, we note that the loss function can capture very well the plasmon peak intensity evolution for the three hybrid plasmon-phonon branches as seen experimentally, featuring two anti-crossings and spectral weight transfer from the low frequency to high frequency plasmon branch (peak 3) with increasing  $q$ .

### III. RESONANCE LINESHAPE AND THE EXTRACTION OF THE PLASMON DAMPING

This section describes the extraction of the plasmon damping rate from the measured extinction spectra, used for Fig. 4 of the main manuscript.



The far-IR plasmon resonance lineshape of graphene micro-disks and ribbons can be well described by a damped oscillator model[19], which is derived from Drude conductivity. In the mid-IR regime, the lineshape becomes asymmetric, as seen for the third peak in Fig. 3a of the main manuscript. Because the lineshape of the resonance peaks in the vicinity of the substrate phonon frequencies might be affected by the plasmon-phonon hybridization, here we focus on the third peak of relatively narrow ribbons on SiO<sub>2</sub> substrate, whose resonance frequency is far away from those of substrate phonons. Fig. S2 shows a spectrum (black curve) of a ribbon array with width  $W = 85$  nm. The spectrum is very asymmetric and a Fano resonance model[20, 21] can well describe it, as shown by the red curve in the figure. In the Fano framework, the extinction spectrum is expressed as

$$1 - \frac{T_{per}}{T_{//}} = \frac{2p}{\pi\Gamma_p(1 + q_f^2)} \frac{(q_f + \eta)^2}{(1 + \eta^2)} \quad (21)$$

where  $p$  is a parameter for the amplitude,  $q_f$  is the Fano parameter,  $\Gamma_p$  is the plasmon damping rate, and  $\eta = 2(\omega - \omega_0)/\Gamma_p$  with  $\omega_0$  being the center frequency. This equation is used to fit the spectra shown in the main manuscript to extract the plasmon damping rate  $\Gamma_p$ . Typical values for Fano parameter  $q_f$  are around 3.

This Fano type resonance indicates that the plasmon resonance is interfered by a broad background continuum. As demonstrated before, the optical conductivity of graphene in the far-IR is Drude like. However, in the mid-IR range we are dealing with here, it's in the Pauli blocking regime, i.e., the optical conductivity has a very weak Drude response tail and some residue conductivity due to many-body effect. It is this residue conductivity serving as the broad continuum to form a Fano type resonance with the plasmon excitation.

#### IV. RESONANCE BROADENING EFFECT DUE TO THE RIBBON WIDTH INHOMOGENEITY

Long wavelength variations in the ribbon's width can also lead to an apparent resonance broadening effect indistinguishable from lifetime broadening effects. In DLC ribbons, the plasmon dispersion is described by a simple  $\omega_{pl}^2 = \alpha q$  dispersion, where  $\alpha \equiv |E_f|e^2/2\pi\hbar^2\epsilon_0\epsilon_{env}$ . In this case, the resonance broadening  $\delta\omega_{pl}$  associated with a character-

istic width inhomogeneity of  $\Delta$  is given by,

$$\delta\omega_{pl} \approx \frac{\sqrt{\alpha}\Delta}{2W_e^{\frac{3}{2}}} \quad (22)$$

In comparison to the plasmon lifetime broadening due to scattering off the edges, it also has a power law behavior of the form  $a/W_e^b$ , the scaling exponent  $b$  in this case is  $\frac{3}{2}$  instead of 1. Fig. S3 plots the experimentally extracted plasmon damping as a function of the effective width  $W_e$  for two different doping levels. Least-square-error fit to the data yields  $b = 1.0$ , indicating that the broadening is due to carrier scattering off the edges. Furthermore, as shown in Fig. S3, there is also no noticeable dependence on doping, where the width inhomogeneity effect would suggest otherwise.

- 
- [1] J. L. Mañes, Phys. Rev. B **76**, 045430 (2007).
  - [2] T. Ando, J. Phys. Soc. Jpn. **75**, 124701 (2006).
  - [3] K. Ishikawa and T. Ando, J. Phys. Soc. Jpn. **75**, 084713 (2006).
  - [4] A. H. Castro Neto and F. Guinea, Phys. Rev. B **75**, 045404 (2007).
  - [5] D. M. Basko, Phys. Rev. B **78**, 125418 (2008).
  - [6] S. Fratini and F. Guinea, Phys. Rev. B **77**, 195415 (2008).
  - [7] J. Schiefele, F. Sols, and F. Guinea, Phys. Rev. B **85**, 195420 (2012).
  - [8] H. Bruus and K. Flensberg, Many-body quantum theory in condensed matter physics, Oxford University Press (2004).
  - [9] G. D. Mahan, Many-particle physics, Springer (2000).
  - [10] E. H. Hwang, R. Sensarma, and S. Das Sarma, Phys. Rev. B **82**, 195406 (2010).
  - [11] B. Wunsch, T. Stauber, F. Sols, and F. Guinea, New Journ. Phys. **8**, 318 (2006).
  - [12] E. H. Hwang and S. D. Sarma, Phys. Rev. B **75**, 205418 (2007).
  - [13] J. Sabio, J. Nilsson, and A. H. C. Neto, Phys. Rev. B **78**, 075410 (2008).
  - [14] L. Ju, B. Geng, J. Horng, C. Girit, M. Martin, Z. Hao, H. A. Bechtel, X. Liang, A. Zettl, Y. R. Shen, et al., Nature Nano. **6**, 630 (2011).
  - [15] F. Koppens, D. E. Chang, and F. J. G. de Abajo, Nano Lett. **11**, 3370 (2011).
  - [16] A. Y. Nikitin, F. Guinea, F. J. Garcia-Vidal, and L. Martin-Moreno, Phys. Rev. B **85**, 081405(R) (2012).
  - [17] M. Jablan, H. Buljan, and M. Soljačić, Phys. Rev. B **80**, 245435 (2009).
  - [18] C. H. Park, F. Giustino, M. L. Cohen, and S. G. Louie, Phys. Rev. Lett. **99**, 086804 (2007).
  - [19] H. Yan, X. Li, B. Chandra, G. Tulevski, Y. Wu, M. Freitag, W. Zhu, P. Avouris, and F. Xia, Nature Nano **7**, 330 (2012).
  - [20] U. Fano, Phys. Rev. **124**, 1866 (1961).
  - [21] Z. Li, C. H. Lui, E. Cappelluti, L. Benfatto, K. F. Mak, G. L. Carr, J. Shan, and T. F. Heinz, Phys. Rev. Lett. **108**, 156801 (2012).

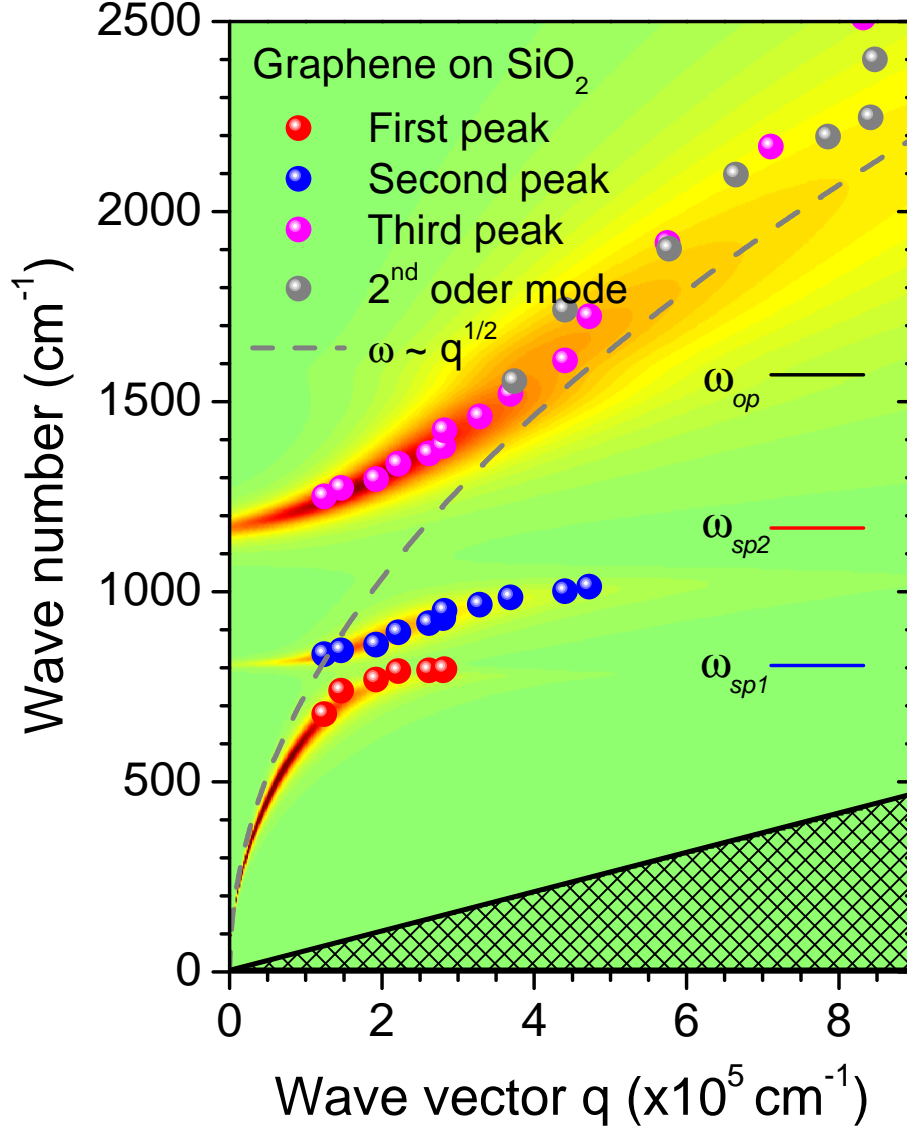


FIG. S 1: **Graphene loss function on SiO<sub>2</sub> substrate.** Calculated RPA loss function  $\Im [1/\epsilon_T^{rpa}]$ , including interactions with the intrinsic and SiO<sub>2</sub> substrate phonons. Graphene doping is assumed to be  $E_f = -0.43$  eV and an effective  $\epsilon_{env} = 1.5$ . Shaded regions represent the intra-band Landau damping regime i.e.  $\hbar\omega/E_f < q/k_F$ . Dashed line on the left plot is calculated from the classical plasmon dispersion  $\omega_{pl}^2 = e^2 q v_F k_F / (2\pi \hbar \epsilon_0 \epsilon_{env})$ . The frequencies of the various phonon modes are assumed to be at  $\omega_{op} = 1580$  cm<sup>-1</sup>,  $\omega_{sp1} = 806$  cm<sup>-1</sup> and  $\omega_{sp2} = 1168$  cm<sup>-1</sup>. The lifetime associated with the phonons used in these plots are  $\tau_{op} = 70$  fs,  $\tau_{sp1} = 0.5$  ps and  $\tau_{sp2} = 0.2$  ps. Calculations include damping of single particle excitations  $\delta_e$  as described in the Suppl. info. text. The coupling parameters used are  $g_0 = 7.7$  eV Å<sup>-1</sup>,  $\mathcal{F}_{sp1}^2 = 0.2$  meV and  $\mathcal{F}_{sp2}^2 = 2$  meV.

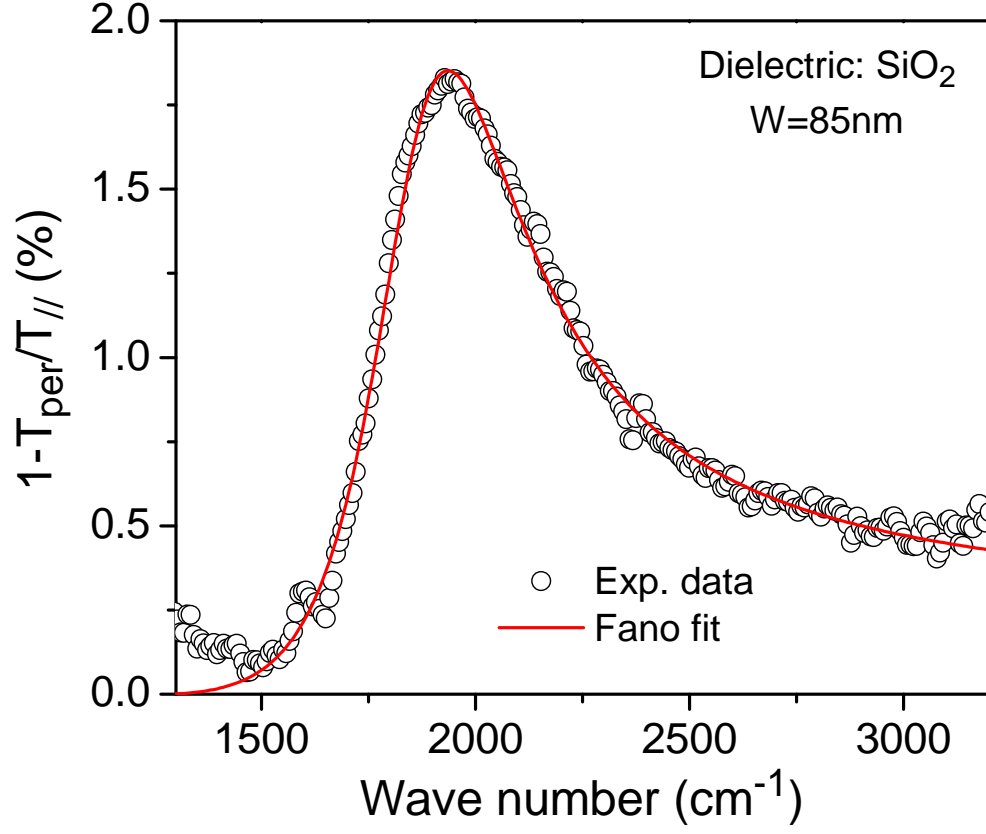


FIG. S 2: **Resonance lineshape and fitting.** Measured extinction spectra of a  $W = 85$  nm ribbon array on SiO<sub>2</sub> substrate, where we show only part of the spectra relating to the peak 3 as described in the main manuscript. The data can be fitted well by a Fano model, with model and parameters described in Suppl. Info text.

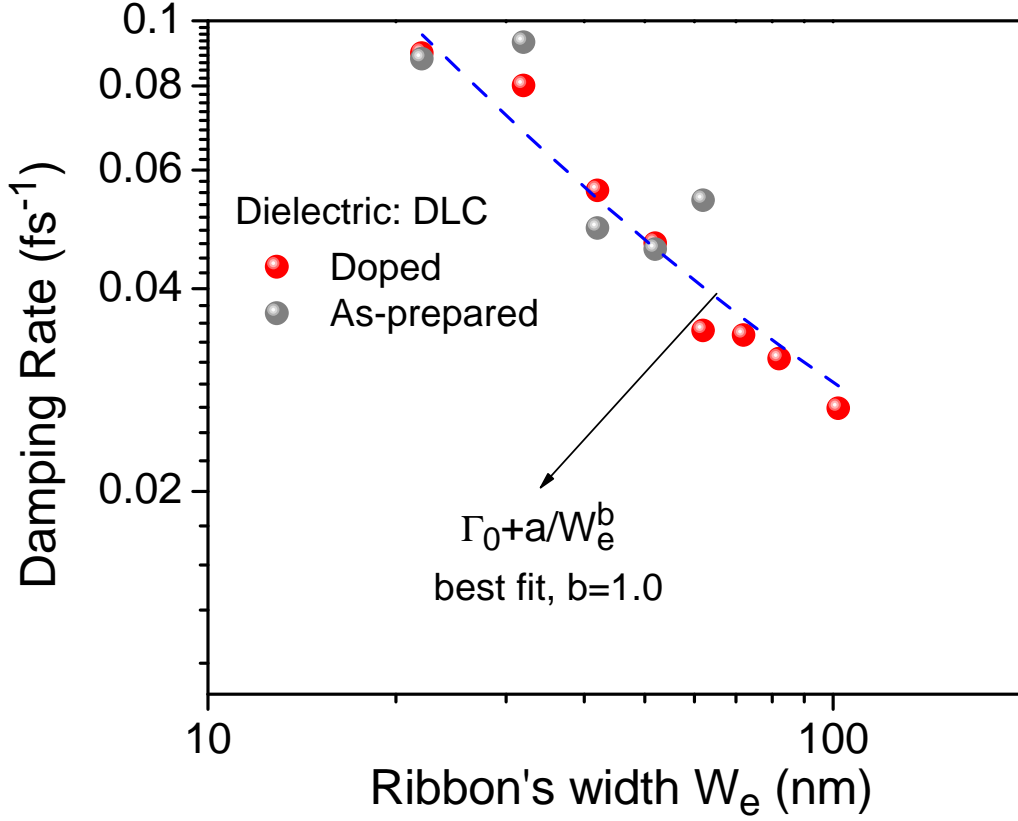


FIG. S 3: **Damping rate scaling with width.** Measured plasmon damping rate in graphene ribbons on DLC substrate as a function of the effective width  $W_e = W - W_0$ , where  $W$  is the physical width and  $W_0 = 28 \text{ nm}$ . See also main text. The plasmon damping rate is best described by the scaling relation  $\Gamma_0 + a/W_e^b$ , where  $\Gamma_0 = 69 \text{ cm}^{-1}$  is related to the background damping, a quantity determined from the Drude response of large area graphene.  $a$  and  $b$  are obtained from least-square-error fit to the experimental data.  $b$  was found to be 1.0.